Analytical and Bioanalytical Chemistry (2019) 411:3979–3988
https://doi.org/10.1007/s00216-019-01883-2

RESEARCH PAPER

Emissions of terbium metal–organic frameworks modulated by dispersive/agglomerated gold nanoparticles for the construction of prostate-specific antigen biosensor

Fei Qu[1,2] · Yanru Ding[1,2] · Xiaoxia Lv[1,2] · Lian Xia[1,2] · Jinmao You[1,2,3] · Wenli Han[4]

Received: 30 January 2019 / Revised: 4 April 2019 / Accepted: 29 April 2019 / Published online: 14 May 2019

Abstract

Herein, a universal and multifunctional fluorescence sensor platform is designed by the interaction of aggregation/dispersion gold nanoparticles (AuNPs) with Tb-metal–organic frameworks (Tb-MOFs). It is found that the dispersed AuNPs rather than the aggregated ones can quench effectively the fluorescence of Tb-MOFs, and the quenching process presumably involves the mechanism of inner filter effect (IFE), dynamic quenching effect (DQE), and fluorescence resonance energy transfer (FRET). The different affinities of aptamer and aptamer–target complex toward AuNPs are employed to modulate the fluorescence signal change of Tb-MOFs. As the proof of concept, prostate-specific antigen (PSA), an efficient tumor indicator for prostate cancer, is selected as the target. At first, the PSA aptamer can protect AuNPs against salt-induced aggregation, leading to the fluorescence of Tb-MOFs quenching. Subsequently, upon PSA introduction, the rigid aptamer–PSA complex is formed and cannot stabilize AuNPs in high salt conditions, so the AuNPs aggregate significantly and the fluorescence of Tb-MOFs is restored. The linear range of PSA is achieved from 1 to 100 ng/mL with a detection limit of 0.36 ng/mL. Finally, this method has been validated to be sensitive and specific for PSA in human urine samples.

Keywords Fluorescence · Metal–organic frameworks · Gold nanoparticles · Prostate-specific antigen · Aptamer

Introduction

Metal–organic frameworks, known as MOFs, are composed of metal ions and organic ligands through strong covalent bonds. As a fascinating class of functional materials, MOFs have been extensively studied for applications in gas storage [1], catalysis [2], separation [3], and drug delivery [4]. Among the large number of MOFs, lanthanide metal–organic frameworks (Ln-MOFs) show unique luminescent properties, including their large Stokes shift, high surface area, long decay lifetime, and well-defined pore structure [5]. Because of the electron-rich ligands, Ln-MOFs are widely used in the sensing applications based on the photoinduced electron transfer (PET) mechanism. For example, the fluorescent Ln-MOFs [6, 7] could be quenched significantly by the explosive nitroaromatic compounds, which were often considered to be a typical kind of electron-deficient molecules. In the effective PET process, the electron-deficient targets are indispensable, while the most of biomolecules are electron-rich partners, such as DNA, enzyme, and protein. Therefore, not a lot of reports are available concerning Ln-MOFs as a platform for sensing biomolecules. Compared with the PET, the inner filter effect (IFE) and fluorescence resonance energy transfer (FRET) are highly popular mechanisms due to the biochemical universality and naturally exceptional s

Electronic supplementary material The online version of this article (https://doi.org/10.1007/s00216-019-01883-2) contains supplementary material, which is available to authorized users.

✉ Fei Qu
qufei3323@163.com

✉ Wenli Han
0904hanwenli@163.com

[1] The Key Laboratory of Life-Organic Analysis, Qufu Normal University, Qufu 273165, Shandong, China

[2] The Key Laboratory of Pharmaceutical Intermediates and Analysis of Natural Medicine, Qufu Normal University, Qufu 273165, Shandong, China

[3] Northwest Institute of Plateau Biology, Chinese Academy of Sciences, Xining 810001, China

[4] Laboratory Animal Center, Chongqing Medical University, Chongqing 404100, China

electivity [8]. By virtue of the IFE and FRET sensing mechanism, many biomolecules have been detected sensitively, including the dopamine [9], glucose [10], glutathione [11], and thrombin [12]. To the best of our knowledge, it is rare for sensing platform focused on the FRET and IFE between MOFs and other analytes, especially for biomolecules. The reason may be attributed to their poor water solubility and lack of recognition sites.

Cancer is one of the most serious diseases that threaten human life and health today. The detection of tumor markers plays a key factor in the early diagnosis of cancer and monitoring treatment response and prognosis. Prostate-specific antigen (PSA), a 34-kDa single-chain glycoprotein, is an efficient tumor indicator for prostate cancer. Typically, most reports about the detection of PSA can be classified into two types: antibody–antigen interaction and aptamer–target molecule interaction. Although antibody–antigen interaction can offer efficient and accurate test results for PSA, the production of antibodies is expensive and time-consuming [13]. On the other hand, aptamer, a single-stranded DNA or RNA possessing highly specific affinity for targets, has the advantages of low-cost and good stability. The binding dissociation constant (K_d) for the interaction of PSA aptamer with PSA is estimated to be several tens of nanomolar [14], revealing that the PSA aptamer has an excellent affinity for PSA. Moreover, it has been widely reported that the aptamer and the aptamer–target complex show different binding abilities to some nanomaterials, such as gold nanoparticles (AuNPs), MoS_2 nanosheets, and graphene oxide (GO) [15–17]. For instance, MoS_2 nanosheet could adsorb dye-labeled aptamer via the van der Waals force and quenched the fluorescence of dye, while the combination of the aptamer to the target PSA induced a robust structure, which was difficult to be adsorbed on the surface of MoS_2, resulting in the release of the aptamer probe and fluorescence restoration [16]. Similarly, through coupling reaction between glutathione-capped quantum dot (QD) and NH_2-modified PSA aptamer, the fluorescence of QD conjugated aptamer could be quenched by GO; when binding with its target PSA, aptamer probe released from the surface of GO and the fluorescence recovery [17]. However, these cases usually involve the labeled or conjugated aptamer, and this may weaken the binding capabilities toward targets and further limit the sensitive measurement [18]. Hence, it is highly demanded to design an aptamer-based and label-free fluorescence sensing approach for PSA determination.

In this study, Tb^{3+} ions and isophthalic acid (isp) as ligand are selected to construct fluorescent Tb-MOFs. The Tb-MOFs synthesized in this paper show an excellent stability in aqueous for a long time, and can also maintain a high level of emissions in high ionic strength and at a wide pH range. Therefore, these favorable features make them potential candidates for the applications in bio-sensing. Interestingly, it is found that the dispersed AuNPs can quench effectively the fluorescence of Tb-MOFs. However, when the AuNPs aggregate significantly in salt condition, the quenching effect is negligible. Several experiments suggest that the interaction between Tb-MOFs and dispersed AuNPs is mainly a dynamic quenching process and involves IFE and FRET. Based on the numerous studies about the interaction between AuNPs and biomolecules, AuNPs can act as the "bridge", which connects the probe of Tb-MOFs and biomolecules as targets. This Tb-MOFs@AuNPs system can be constructed as a universal and multifunctional platform. On the basis of the high affinity of aptamer toward its target, a label-free aptasensor for PSA is designed. In the absence of PSA, the aptamer can stabilize AuNPs against salt-induced aggregation, leading to the fluorescence of Tb-MOFs quenching. Upon binding to PSA, the aptamer specifically reacts with its target PSA with a conformational change from flexible structure to a rigid structure, which cannot adsorb on the surface of AuNPs, so in the high salt state, the AuNPs tend to aggregate and the emissions of Tb-MOFs recover. The proposed method shows a wide line range of PSA from 1 to 100 ng/mL with the limit of detection (LOD) of 0.36 ng/mL. Furthermore, this work has been successfully applied for detecting PSA in human urine samples with satisfactory recoveries compared with enzyme-linked immunosorbent assay (ELISA) as a reference.

Experiment

Chemicals and reagents

Terbium(III) chloride hexahydrate ($TbCl_3 \cdot 6H_2O$), isophthalic acid (isp), sodium citrate ($Na_3C_6H_5O_7$), chloroauric acid ($HAuCl_4$), N,N-dimethylformamide (DMF), sodium chloride (NaCl), Tris (hydroxymethyl) amino methane (Tris), hydrochloric acid (HCl), urea, uric acid, human serum albumin (HSA), trypsin, thrombin, IgG, urease, lysozyme, histidine, L-leucine, L-arginine, lysine, L-threonine, sucrose, glucose, D-mannose, fructose, Na_2HPO_4, KNO_3, $ZnCl_2$, $CaCl_2$, and $MgCl_2$ were obtained from Aladdin (Shanghai, China). Prostate-specific-antigen (PSA) from human was purchased from Sigma. A PSA ELISA kit was purchased from Jiangsu Baolai Biotechnology Co., LTD. (Nanjing, China). The PSA aptamer (5′-TTATTAAAGCTCGCCATCAAATAGC-3) was synthesized by Sangon Biotechnology Co. Ltd. (Shanghai, China). Human urine samples of healthy volunteers were provided from the local hospital. Ultrapure water was prepared with throughout the whole experiment.

Instruments

The fluorescence spectra were recorded on a Hitachi F-7000 fluorescence spectrophotometer (Tokyo, Japan). A Cary 300 Bio UV-vis spectrophotometer was used to monitor the UV–

vis absorption spectra. JEM-2100F electron microscope was applied to record the transmission electron microscopy (TEM) images and energy-dispersive X-ray spectroscopy (EDS) patterns. X-ray diffraction (XRD) spectrum was obtained on powder diffractometer (MiniFlex600 X-ray) and the Fourier transform infrared (FT-IR) spectrum was recorded from Thermo Nicolet Nexus 470 FT-IR ESP spectrometer. The fluorescence lifetimes were recorded using a photo-counting system from Quantaurus-Tau C11367–11 (Hamamatsu) with laser excitation at 280 nm. Zeta potential was performed using a Zetasizer Nano ZS-90 (Malvern Instruments, Malvern, UK). Dynamic light scattering (DLS) experiment was obtained with ALV 500 laser light scattering instrument.

Preparation of Tb-MOFs

The Tb-MOFs were synthesized according to the previous method [19]. Briefly, $TbCl_3{\cdot}6H_2O$ (0.10 mmol, 37.3 mg) and isp (0.1 mmol, 16.6 mg) were added in DMF/H_2O (7:3 *v*/*v*) solution and stirred for 2 h. Next, the mixture was sealed in a Teflon vessel in a stainless steel autoclave and reacted at 150 °C for 12 h and then cooled down to room temperature slowly. Finally, the products were collected by centrifugation and washed with DMF and ethanol several times. After dried at room temperature, the Tb-MOFs were obtained.

Synthesis of AuNPs

These AuNPs were synthesized by citrate reduction method [20]. At first, aqua regia (mixture of HCl and HNO_3 at a 3:1 ratio) was used to wash all glassware and magnetic stirrer bars. Typically, 0.01 g $HAuCl_4$ was dissolved to 95 mL deionized water under stirring. When the solution was heated to boil, the sodium citrate solution (5 mL, 0.01% (*w*/*v*)) was added to the mixture until the color turns to wine red. Then, it was cooled to room temperature and preserved at 4 °C for future use. By calculating, the concentration of AuNPs solution was approximately 2.5 nM according to an extinction coefficient of 3.87×10^8 M^{-1} cm^{-1} at 420 nm [21].

Fluorescent detection of PSA

First, the PSA aptamer was dissolved in aqueous solutions and heated to 95 °C for 5 min and then immediately cooled in ice for 20 min before use. Next, 50 μL PSA aptamer (1 mM) was added into 100 μL Tris-HCl buffer (pH 7.4, 20 mM). Then, PSA (1–100 ng/mL) was dissolved into the above mixture and incubated at 37 °C for 30 min. Subsequently, 200 μL AuNPs (2.5 nM) was added to the solution with vigorous stirring for 5 min. Next, 50 μL NaCl (1 M) was added to achieve ultimate concentration of 50 mM. After reacted for 5 min, 200 μL of Tb-MOFs solution (0.1 mg/mL) was added into the above mixture with a final volume of 1 mL and the fluorescence spectra of the samples were collected with excitation at 280 nm. The change of fluorescence intensity was expressed as $F_2 - F_1$, where F_1 and F_2 represented the fluorescence intensities of Tb-MOFs@AuNPs@aptamer system at 545 nm in the absence and presence of PSA, respectively. Generally, LOD is defined as the concentration of analyte that corresponds to three times the signal-to-noise ratio ($S/N = 3$) [22]. LOD is calculated according to the expression $LOD = 3\sigma/K$, where σ is the standard deviation for the blank solution ($n = 10$) and K is the slope of the calibration curve.

Real sample detection

In brief, 5 mL of urine samples was centrifuged at 4000 rpm (3800×*g*) for 15 min. Next, the supernatant of sample was diluted 100-fold with ultrapure water. Finally, different concentrations of PSA standard solutions were spiked into the samples. Other steps were completed as described above. As a control experiment, urine samples were examined by the standard ELISA.

Results and discussion

Characterization of Tb-MOFs and AuNPs

The Tb-MOFs are prepared with Tb^{3+} ions and isophthalic acid (isp) as ligand. Upon the excitation of 280 nm (Fig. 1a), the Tb-MOFs exhibit the four characteristic emission peaks of Tb^{3+} at 488, 545, 584, and 619 nm, which are arisen from the $^5D_4$ excited states to ground states of ^7F_J ($J = 6, 5, 4, 3$) transitions of Tb^{3+} ions, respectively [23]. The solution of Tb-MOFs is colorless under day light, while emits a bright yellow-green fluorescence under UV light at 254 nm (inset in Fig. 1a). Moreover, the Tb-MOFs with well-dispersed distribution exhibit an approximate flake morphology in TEM image (Fig. 1b), and DLS analysis demonstrates that the average size of Tb-MOFs is 505.9 nm (see Electronic Supplementary Material (ESM) Fig. S1). The EDS result shows that the synthesized Tb-MOFs contain elements C, O, and Tb (ESM Fig. S2), indicating that Tb-MOFs are composed of isp and Tb^{3+} ions. The XRD pattern of the Tb-MOFs is in good agreement with the simulation (Fig. 1c), and it also reveals that Tb-MOFs have isomorphic and phase purity with high crystallinity. Compared with the FT-IR spectrum of free isp, the Tb-MOFs do not display a characteristic peak of carboxylic acid structure at 1695 cm^{-1} for C=O stretching vibration, so the carboxylate groups of isp coordinate to Tb^{3+} to form Tb-MOFs (Fig. 1d). All these results prove the successful synthesis of Tb-MOFs.

Subsequently, the stability of these Tb-MOFs has been investigated in detailed. As depicted in ESM Fig. S3, the Tb-MOFs are obtained as white powders and can be well

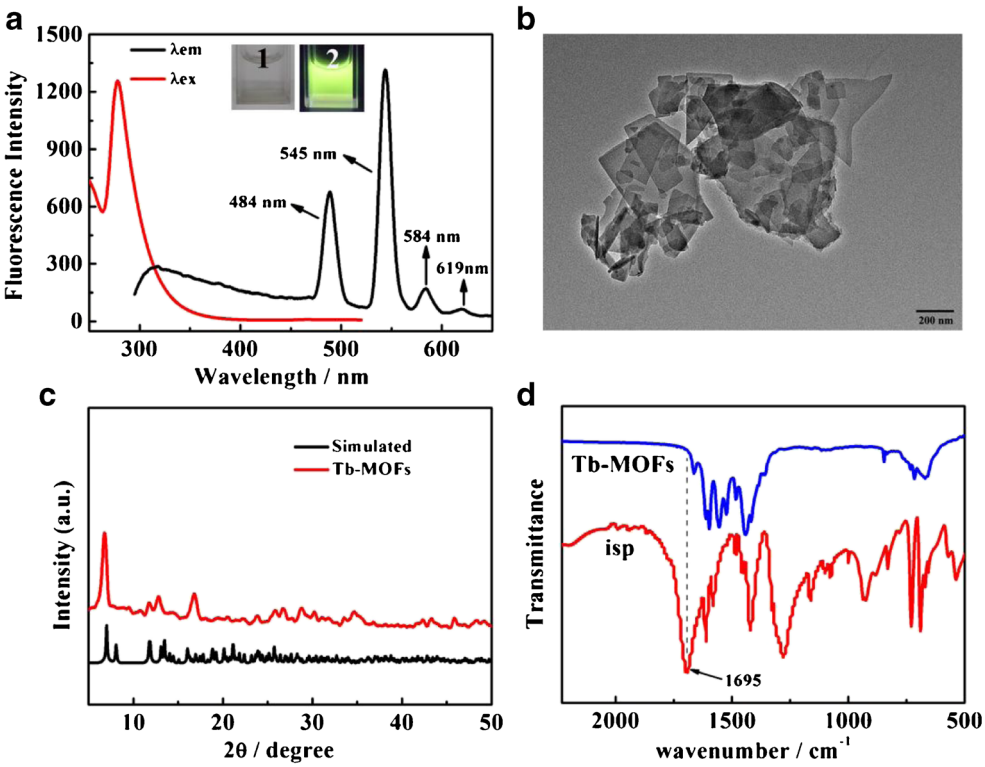

Fig. 1 Excitation and the emission spectra of Tb-MOFs (λex = 280 nm, λem = 545 nm) (**a**); TEM image of Tb-MOFs (**b**); XRD patterns of the Tb-MOFs and the simulated (**c**); FT-IR spectra of isp and Tb-MOFs (**d**). The insets of (**a**) are photographs of Tb-MOFs solution under daylight (1) and UV light at 254 nm (2)

dispersed in water medium. Most importantly, the emissions of Tb-MOFs solution can keep stable for at least 1 week (ESM Fig. S4), and the high ionic strength also shows a negligible effect on Tb-MOFs (ESM Fig. S5). Furthermore, the Tb-MOFs exhibit a high level of emissions at a wide pH range from 3 to 12, but are quenched in strong acid and alkali conditions (ESM Fig. S6). The superior stability of this kind of Tb-MOFs particularly makes them a promising candidate for the applications in bio-sensing.

Besides, the citrate-protected AuNPs with the typical wine red color are also successfully fabricated, and they can highly disperse in aqueous solution due to the negatively charged citrate ions. The surface plasmon resonance (SPR) peak of AuNPs appears at 520 nm (ESM Fig. S7a), and the average diameter of these particles is about 18.25 nm ± 0.52 nm by averaging the size of 50 dots in TEM image (ESM Fig. S7b).

The interaction between Tb-MOFs and AuNPs

As shown in Fig. 2a, with the addition of AuNPs, the fluorescent signal of Tb-MOFs can be efficiently quenched in 5 min, illustrating that the interaction between Tb-MOFs and AuNPs is fast. At the same time, Tb-MOFs cannot induce the aggregation of AuNPs, which maintain the wine red color (ESM Fig. S8). The quenching efficiency is positive correlation to the concentration of AuNPs, and when the concentration of AuNPs is 0.5 nM, the fluorescence of Tb-MOFs approximately drops to 65% (Fig. 2b). Massive AuNPs make an unfavorable effect for the sensitive detection of target, so 0.5 nM of AuNPs solution is selected for this experiment. However, AuNPs agglomerate obviously in the presence of salt. With increasing the concentration of NaCl, the SPR band of AuNPs around 520 nm decreases and a new absorption peak located at 680 nm appears accompanying with solution color changing from wine red to blue (Fig. 2c). Interestingly, following the gradual aggregation of AuNPs, the fluorescence of Tb-MOFs recovers (Fig. 2d). Herein, 50 mM NaCl is chosen for the subsequent experiment.

By comparison of the absorption spectra of dispersed or aggregated AuNPs with the excitation and emission spectra of Tb-MOFs in Fig. 3a, it can be seen clearly the dispersed AuNPs show a broad absorption in the region of 250–600 nm with a SPR peak located at 520 nm, while the aggregated AuNPs in salt solution display a remarkable red-shifting of SPR peak from 520 to 680 nm, and the absorbance at the wavelength from 250 to 400 nm weakens. It means that the dispersed AuNPs rather than the aggregated ones have a good spectral overlap with the excitation and emission band of the Tb-MOFs. Therefore, IFE is firstly considered for the fluorescence quenching of Tb-MOFs by the dispersed AuNPs. The role of IFE among the quenching process is investigated according to Eq. 1 described as below [24]:

$$\frac{F\mathrm{cor}}{F\mathrm{obsd}} = \frac{2.3dA\mathrm{ex}}{1-10^{-dA\mathrm{ex}}}\,10^{gA\mathrm{em}}\,\frac{2.3sA\mathrm{em}}{1-10^{-sA\mathrm{em}}} \quad (1)$$

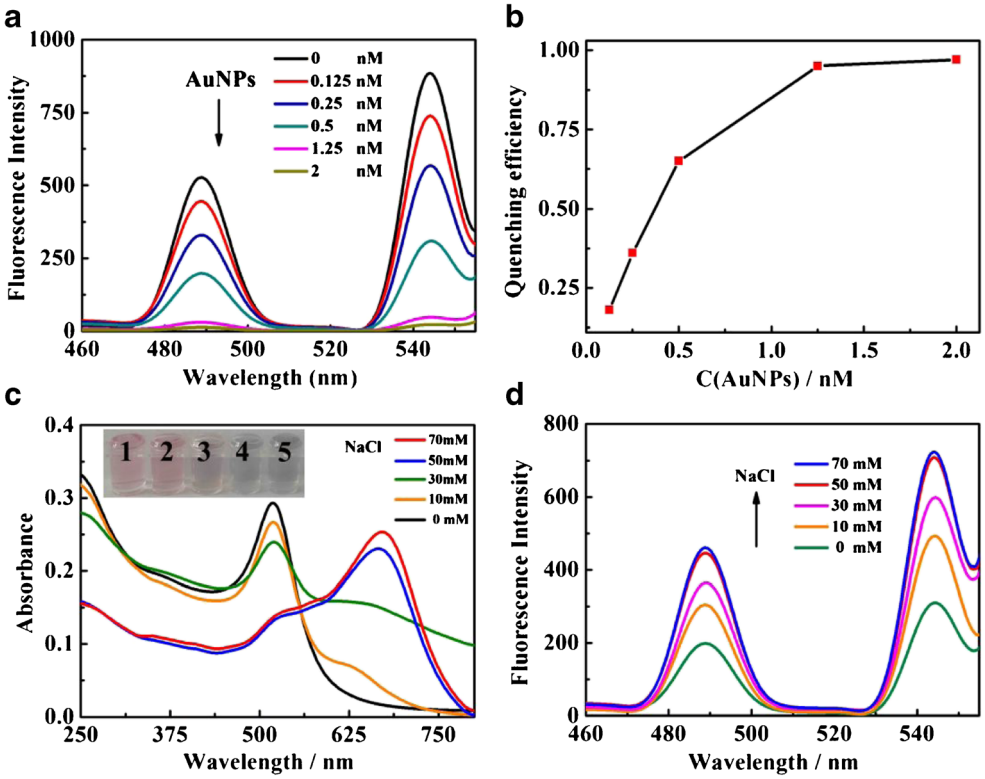

Fig. 2 Fluorescence spectra of Tb-MOFs upon the addition different concentrations of AuNPs (**a**) and the corresponding quenching efficiency (**b**); UV–vis absorption spectra of AuNPs upon the addition different concentrations of NaCl (**c**). Fluorescence spectra of Tb-MOFs@AuNPs system upon the addition of different concentrations of NaCl (**d**). The inset of (**c**) is the corresponding photographs, and the concentrations of NaCl in photograph from 1 to 5 are 0, 10, 30, 50, and 70 mM, respectively. The concentration of Tb-MOFs is 0.02 mg/mL. All data are recorded at the emission of 545 nm with the excitation at 280 nm

where F_{obsd} is the measured maximum fluorescence intensity of Tb-MOFs with the addition of AuNPs at 545 nm and F_{cor} is the corresponding corrected maximum fluorescence intensity by removing IFE from F_{obsd}; A_{ex} and A_{em} are the absorbance of Tb-MOFs with the addition of AuNPs at the excitation wavelength ($\lambda ex = 280$ nm) and maximum emission wavelength ($\lambda em = 545$ nm), respectively; s is the thickness of excitation beam (0.10 cm); d is the width of the cuvette (1.00 cm); and g is the distance between the edge of the excitation beam and the edge of the cuvette (0.40 cm in this case). The maximum value of the correction factor (CF) cannot exceed 3; otherwise, the correction is not convincing.

As displayed in ESM Table S1, the CF of IFE and the relevant parameters change with increasing the concentration of quencher at various temperatures. By calculating the observed and corrected suppressed efficiency (E%) of Tb-MOFs after adding different amounts of AuNPs (Fig. 3b), it is found that approximate 20% of the quenching effect is attributed to the IFE at 293 K. After removing the IFE, the remaining quenching effect may lead to the fluorescence decrease of Tb-MOFs.

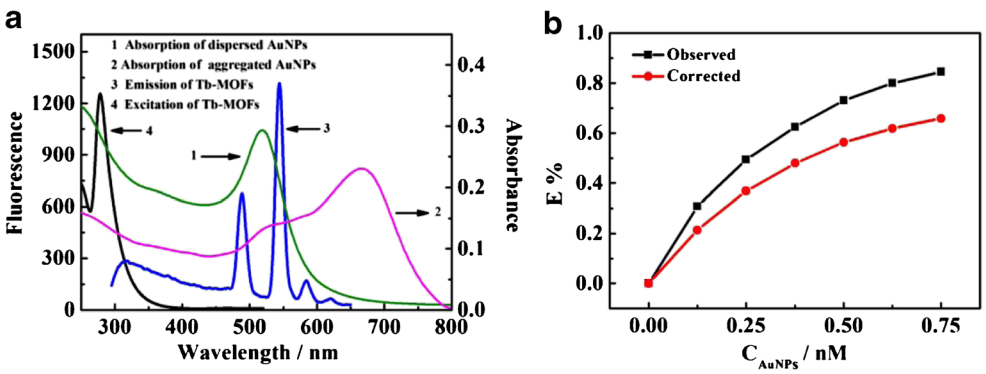

Fig. 3 Comparison of absorption spectra of dispersed or aggregated AuNPs with the excitation and emission spectra of free Tb-MOFs (**a**). Suppressed efficiency (E%) of observed (black line, E_{obsd}%) and corrected (red line, E_{cor}%) results for Tb-MOFs after each addition of various concentrations of AuNPs at room temperature (**b**). $E_{obsd} = 1 -$ F_{obsd} $F_{obsd,0}$, in which $F_{obsd,0}$ is the observed fluorescence intensity of Tb-MOFs in the absence of AuNPs. $E_{cor} = 1 - F_{cor}$ $F_{cor,0}$, in which $F_{cor,0}$ is the corrected fluorescence intensity of Tb-MOFs in the absence of AuNPs. The concentration of Tb-MOFs is 0.02 mg/mL. The data are recorded at 545 nm with the excitation at 280 nm

Subsequently, the static quenching effect (SQE) and dynamic quenching effect (DQE) are analyzed for the quenching mechanism by Stern–Volmer equation [25] (Eq. 2):

$$\frac{F0}{F} = 1 + Ksv[Q] \quad (2)$$

where F_0 and F are the fluorescence intensity of Tb-MOFs before and after adding the AuNPs; K_{SV} is the Stern–Volmer quenching constant, and $[Q]$ is the concentration of AuNPs. In this assay, because of removing the IFE effect, the F_0 and F should be replaced with the $F_{cor,0}$ and F_{cor}, which are the corrected fluorescence intensities of Tb-MOFs in the absence and presence of AuNPs according to Eq. 1 (given in ESM Table S1). As shown in ESM Fig. S9, the corrected fluorescence intensity ratios linearly respond to the concentration of AuNPs at different temperatures. The liner Stern–Volmer plot usually indicates that one type of quenching mechanism (SQE or DQE) is predominating [26]. Moreover, the SQE and DQE can be differentiated by their dependence on temperature. In dynamic quenching process, increasing temperature will accelerate the collision between the quencher and the fluorophore, resulting in the K_{SV} increasing. The obtained K_{SV} from Stern–Volmer slope at 293, 303, and 313 K are 2.629×10^9, 5.466×10^9, and 1.36×10^{10} M^{-1}, respectively. The results coincide with DQE, indicating that the interaction between Tb-MOFs and AuNPs is mainly a dynamic quenching process.

To further explore the quenching mechanism, FRET in quenching effect is further investigated due to the good spectral overlap between absorption spectrum of dispersed AuNPs and emission spectrum of Tb-MOFs. As well known, one of the most important differences between FRET and IFE is that fluorescence lifetime of the donor will change in the FRET, but it will not in the IFE [27]. The fluorescence decays of Tb-MOFs in the absence and presence of dispersed AuNPs are calculated according to ESM Fig. S10a by using Eq. 3 [28].

$$\langle \tau \rangle = \sum_i fi\tau i \quad (3)$$

The fluorescence decay of Tb-MOFs changes from 2.31 to 1.05 ns after adding dispersed AuNPs, revealing that the fluorescence quenching of Tb-MOFs by dispersed AuNPs may be ascribed to FRET. For an effective FRET, a substantial spectral overlap between the donor emission and the acceptor absorption is required, so the Tb-MOFs act as the donor and the dispersed AuNPs are the effective acceptor. Furthermore, the FRET efficiency is related to the distance between the donor and the acceptor [25]. In ESM Fig. S10b, the zeta potential of dispersed AuNPs is − 68.6 mV at pH 7.4, indicating that dispersed AuNPs are negatively charged due to the citrate ions coating on the surface of AuNPs. While Tb-MOFs are + 13.3 mV; as a result, the negatively charged AuNPs can interact with the positively charged Tb-MOFs via the electrostatic attraction interaction, which shortens the distance between dispersed AuNPs and Tb-MOFs. These results verify the effective FRET from Tb-MOFs to dispersed AuNPs. Besides, TEM image also validates that a lot of AuNPs can adsorb onto the surface of large Tb-MOFs flakes (ESM Fig. S10c). EDS pattern shows that the Tb-MOFs@AuNPs is comprised of C, O, Au, and Tb of 24.83, 15.57, 6.10, and 19.47 wt% concentration, respectively (ESM Fig. S11), suggesting that the content ratio of Tb-MOFs and AuNPs in the Tb-MOFs@AuNPs system is about 3.19:1. Hence, the fluorescence quenching of Tb-MOFs by dispersed AuNPs presumably involves the process of IFE, DQE, and FRET.

Detection of PSA based on the Tb-MOFs@AuNPs platform

It has been reported that single-stranded DNA (ssDNA) with a random sequence can be easily adsorbed on the surface of AuNPs and protect AuNPs against salt-induced aggregation, because the inter-particle electrostatic repulsion between ssDNA-adsorbed AuNPs becomes stronger in comparison with the free AuNPs [29]. Hence, several ssDNA with different sequences (ESM Table S2), including PSA aptamer, ATP aptamer (ABA), human immunodeficiency virus (HIV) DNA, hepatitis B virus (HBV) DNA, thrombin aptamer (TBA), and telomere DNA (Tel 22), are selected to investigate the protective effect of ssDNA on AuNPs. As shown in ESM Fig. S12, all of these ssDNA can stabilize AuNPs against aggregation at high salt concentration, indicating that the AuNPs exhibit no selectivity to the nucleic acid molecules. However, when the ssDNA is an aptamer that is specific to its target, the assay displays a good selectivity. Due to the formation of aptamer–target complex, a rigid structure avoids binding of the DNA bases on AuNPs surface [29], so the AuNPs aggregate again in high salt condition (ESM Fig. S13). It means that the target and aptamer modulate the dispersive or aggregated state of AuNPs in salt solution, and these AuNPs can act as the "bridge," which connects the probe of Tb-MOFs and biomolecules as targets (Scheme 1). As the proof of concept, PSA, an efficient tumor indicator for prostate cancer, is selected as the target in this assay.

As shown in Fig. 4, compared with the free Tb-MOFs (line 1), the quenching abilities of the dispersed AuNPs and aggregated ones are different (lines 2 and 3). The PSA aptamer stabilized AuNPs can keep dispersive in the presence of salt, producing the emissions quenching of Tb-MOFs (line 4). Subsequently, when the aptamer specifically reacts with its target PSA and forms aptamer–PSA complex, which shows a rigid structure and cannot protect

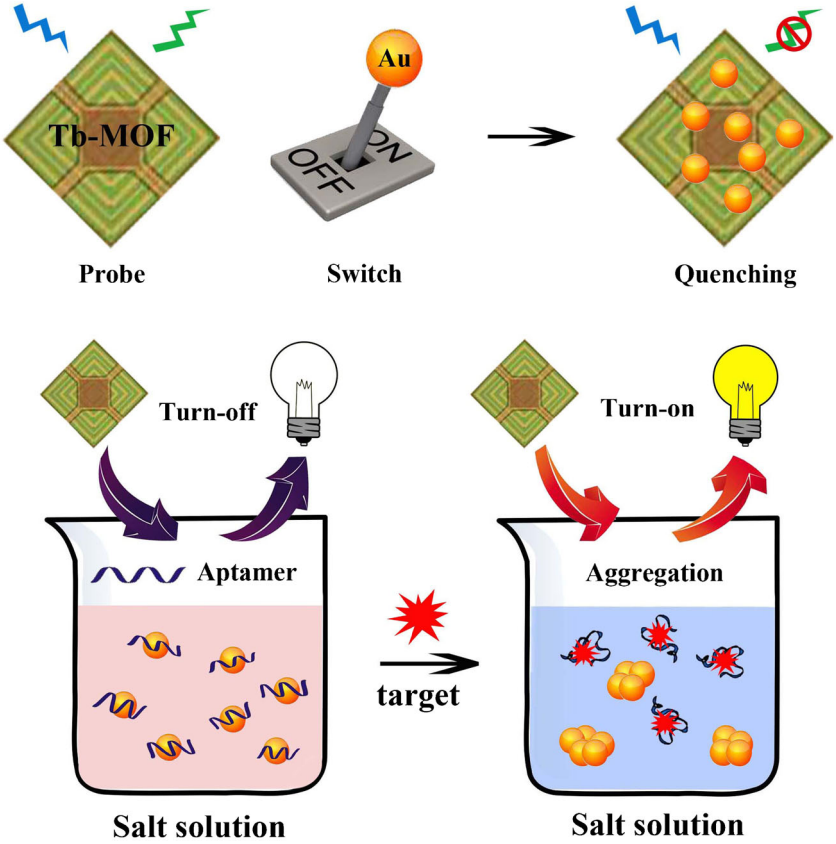

Scheme 1 Schematic illustration of construction of aptasensor based on the interaction of Tb-MOFs with dispersive/agglomerated AuNPs

AuNPs on the high salt condition, so the aggregation of AuNPs induces the recovery of Tb-MOFs (line 5). In this case, Tb-MOFs play the role of probe, AuNPs as the switch and aptamer as the identification element.

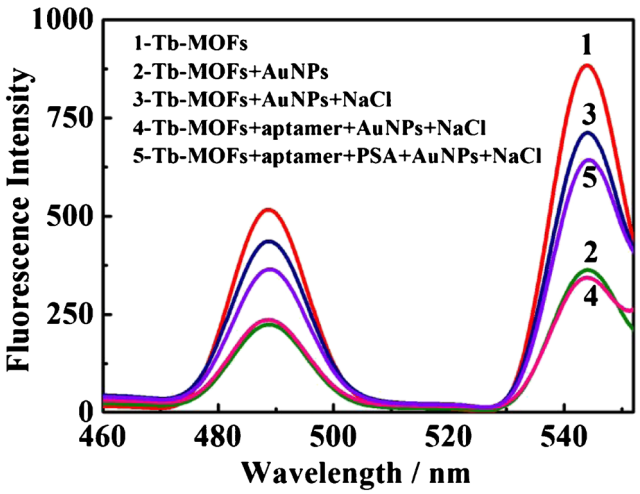

Fig. 4 Fluorescence spectra of free Tb-MOFs (line 1) and Tb-MOFs in the presence of AuNPs (line 2); both AuNPs and NaCl (line 3); the mixture of aptamer, AuNPs, and NaCl (line 4); and the mixture of aptamer, PSA, AuNPs, and NaCl (line 5) in Tris-HCl buffer (pH 7.4). The concentrations of Tb-MOFs, AuNPs, NaCl, aptamer, and PSA are 0.02 mg/mL, 0.5 nM, 50 mM, 50 nM, and 100 ng/mL, respectively. The excitation wavelength is 280 nm

Sensitivity

The concentration of aptamer is an important factor for effectively protecting AuNPs and sensitively responding to PSA. As depicted in ESM Fig. S14, 50 nM of aptamer can provide the effective protection of AuNPs against salt-induced aggregation. Thus, 50 nM of aptamer is chosen for sensitive detection of PSA. Next, the fluorescence change of Tb-MOFs@AuNPs system in the presence of aptamer and NaCl with addition of various concentrations of PSA is recorded in Fig. 5. With increasing the concentration of PSA, the fluorescence of Tb-MOFs enhances gradually, and the linear range of PSA is obtained from 1 to 100 ng/mL with LOD of 0.36 ng/mL. The comparison of this paper with other reports for PSA detection (in ESM Table S3) suggests that this method is not inferior to other assays and exhibits a relatively wide linear range and low limit detection.

Selectivity

It is well known that human urine usually contains a large number of metabolites, such as amino acids, urea, uric acid, inorganic salts, sugars, and some proteins [30]. To evaluate the specificity for PSA, some potential interference substances are exploited, including urea, uric acid, HSA, trypsin, thrombin, IgG, urease, lysozyme, histidine, L-leucine, L-arginine, lysine,

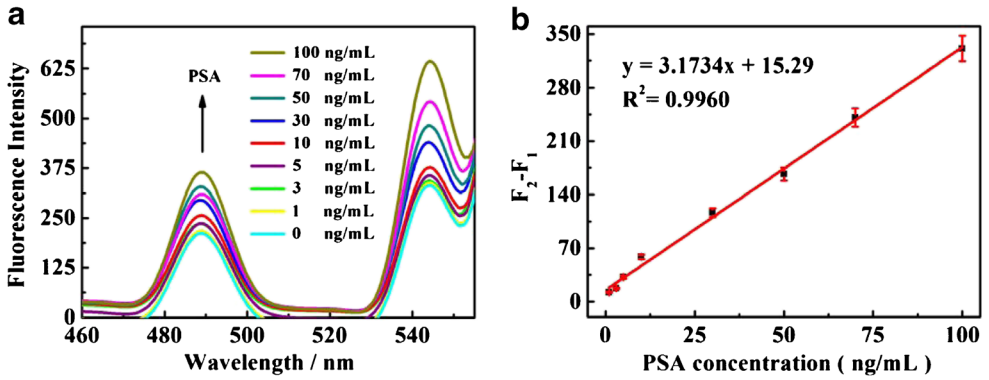

Fig. 5 Fluorescence spectra of Tb-MOFs@AuNPs system in the presence of NaCl and aptamer with addition of different concentrations of PSA (**a**) and corresponding linear range of PSA (**b**) in Tris-HCl buffer (pH 7.4). The concentrations of Tb-MOFs, AuNPs, NaCl and aptamer are 0.02 mg/mL, 0.5 nM, 50 mM, and 50 nM, respectively. The excitation wavelength is 280 nm and all data are recorded at the emission of 545 nm

L-threonine, sucrose, glucose, D-mannose, fructose, Cl^-, HPO_4^{2-}, NO_3^-, Zn^{2+}, Ca^{2+}, Mg^{2+}, K^+, and Na^+. As shown in Fig. 6, a distinct fluorescence variation induced by PSA can be observed, while other substances are invalid. The results indicate that this method based on the high specific reaction between aptamer and PSA has excellent selectivity.

PSA determination in real sample

Compared with the traditional assessments of serum PSA, it is proved that detection of urinary PSA has become a credible candidate. Especially, prostatitis and benign prostatic hyperplasia will also produce the high serum PSA in benign conditions, resulting in the inaccurate values [31]. Therefore, the levels of PSA in urine samples are analyzed by the proposed method, and ELISA is selected as a reference method. The experimental results are obtained by using the standard addition method as described in Table 1. The desirable recoveries of PSA in human urine samples are from 96 to 109% for the proposed method and 97 to 103% for ELISA. There is no significant difference between the two methods, indicating the well applicability of this biosensor to quantitative detection of PSA in real biological matrices.

Conclusion

Herein, the stable Tb-MOFs with good water dispersion are developed. By using the good quenching effect of dispersive AuNPs on the Tb-MOFs, a label-free aptasensor for PSA is constructed based on Tb-MOFs@AuNPs sensing platform. Due to the protection of aptamer, the AuNPs can be dispersive

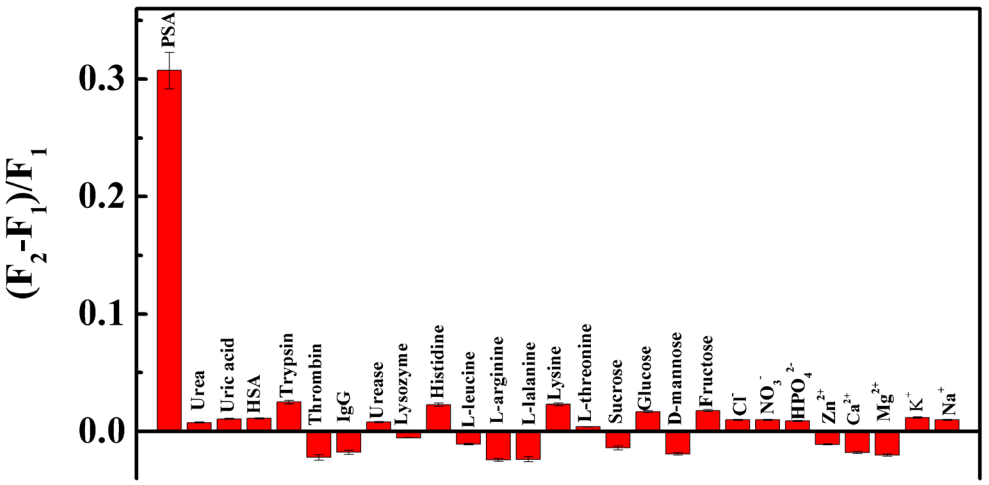

Fig. 6 Selectivity of the detection of PSA over other interference substances in Tris-HCl buffer (pH 7.4). The concentration of PSA is 30 ng/mL; the concentrations of uric acid, HSA, trypsin, thrombin, IgG, urease, lysozyme, histidine, L-leucine, L-arginine, lysine, L-threonine, Zn^{2+}, Ca^{2+}, and Mg^{2+} are 300 ng/mL. The concentrations of sucrose, glucose, D-mannose, fructose, and HPO_4^{2-} are 1 mg/mL. The concentrations of urea, Cl^-, NO_3^-, K^+, and Na^+ are 2 mg/mL. The concentrations of Tb-MOFs, AuNPs, NaCl, and aptamer are 0.02 mg/mL, 0.5 nM, 50 mM, and 50 nM, respectively. All data are recorded at the emission of 545 nm with the excitation at 280 nm

Table 1 Determination of PSA in urine samples by proposed method and ELISA

PSA	Proposed method			Reference method (ELISA)		
Added (ng/mL)	Found (ng/mL)	Recovery (%)	RSD ($n = 3$, %)	Found (ng/mL)	Recovery (%)	RSD ($n = 3$, %)
0	–	–	–	–	–	–
10	10.9	109	0.6	10.23	102.3	0.4
30	30.27	100.9	1.3	31.09	103.6	1.6
50	49.31	98.6	0.9	48.99	97.98	0.7
70	67.69	96.7	1.7	68.59	97.99	1.3

in high salt condition and quench the fluorescence of Tb-MOFs. With addition of PSA, the aptamer–target complex releases from AuNPs, which aggregate significantly in salt solution, causing the emission recovery of Tb-MOFs. Compared with other ways involving labeled aptamer, this strategy not only costs less and operates easily but also displays satisfactory sensitivity and selectivity. Last but not least, this work supplies a new and general MOFs-based protocol that can be extended for probing numerous other biological targets by changing the sequence of aptamer.

Funding information This work was supported by the National Natural Science Foundation of China (Youth Fund Project) (21405093), the Scientific Research Foundation of Qufu Normal University (BSQD20130117), the Experimental Research Project of Qufu Normal University (jp201716), and Higher Educational Science andTechnology Program of Shandong Province, China (Grant No. J15LC04).

Compliance with ethical standards

Conflict of interest The authors declare that they have no conflict of interest.

Ethical committee approval Urine sample experiments were performed according to the Guidelines for Ethical Committee, Qufu Normal University. All urine samples were from healthy volunteers with their informed consent. All studies were approved by Ethical Committee, Qufu Normal University.

References

1. Gándara F, Furukawa H, Lee S, Yaghi OM. High methane storage capacity in aluminum metal–organic frameworks. J Am Chem Soc. 2014;136(14):5271–4.
2. Fei H, Cohen SM. Metalation of a thiocatechol-functionalized Zr (IV)-based metal–organic framework for selective C–H functionalization. J Am Chem Soc. 2015;137(6):2191–4.
3. Kang ZX, Fan LL, Sun DF. Recent advances and challenges of metal–organic framework membranes for gas separation. J Mater Chem A. 2017;5(21):10073–91.
4. Zheng HQ, Zhang YN, Liu LF, Wan W, Guo P, Nyström AM, et al. One-pot synthesis of metal–organic frameworks with encapsulated target molecules and their applications for controlled drug delivery. J Am Chem Soc. 2016;138(3):962–8.
5. Hu ZC, Deibert BJ, Li J. Luminescent metal-organic frameworks for chemical sensing and explosive detection. Chem Soc Rev. 2014;3(16):5815–40.
6. Zhang F, Wang Y, Chu TS, Wang ZH, Yang YY. A facile fabrication of electrodeposited luminescent MOF thin films for selective and recyclable sensing of nitroaromatic explosives. Analyst. 2016;(14, 14):4502–10.
7. Qin JH, Ma B, Liu XF, Lu HL, Dong XY, Zang SQ, et al. Ionic liquid directed syntheses of water-stable Eu- and Tb-organic-frameworks for aqueous-phase detection of nitroaromatic explosives. Dalton Trans. 2015;44(33):14594–603.
8. Medintz IL, Clapp AR, Mattoussi H, Goldman ER, Fisher B, Mauro JM. Self-assembled nanoscale biosensors based on quantum dot FRET donors. Nat Mater. 2003;2(9):630.
9. Uppa Y, Ngamdee K, Promarak V, Ngeontae W. Fluorescence chemodosimeter for dopamine based on the inner filter effect of the in situ generation of silver nanoparticles and fluorescent dye. Spectrochim. Acta, Part A 2018;200:313–321.
10. Chen HY, Fang AJ, He L, Zhang YY, Yao SZ. Sensitive fluorescent detection of H2O2 and glucose in human serum based on inner filter effect of squaric acid-iron (III) on the fluorescence of upconversion nanoparticle. Talanta. 2017;164:580–7.
11. Huang YY, Zhou J, Feng H, Zheng JY, Ma HM, Liu WD, et al. A dual-channel fluorescent chemosensor for discriminative detection of glutathione based on functionalized carbon quantum dots. Biosens Bioelectron. 2016;86:748–55.
12. Wang YH, Bao L, Liu ZH, Pang DW. Aptamer biosensor based on fluorescence resonance energy transfer from upconverting phosphors to carbon nanoparticles for thrombin detection in human plasma. Anal Chem. 2011;83(21):8130–7.
13. Yang K, Hu YJ, Dong N, Zhu GC, Zhu TF, Jiang NJ. A novel SERS-based magnetic aptasensor for prostate specific antigen assay with high sensitivity. Biosens Bioelectron. 2017;94:286–91.
14. Savory N, Abe K, Sode K, Ikebukuro K. Selection of DNA aptamer against prostate specific antigen using a genetic algorithm and application to sensing. Biosens Bioelectron. 2010;26(4):1386–91.
15. Chen ZG, Lei YL, Chen X, Wang Z, Liu JB. An aptamer based resonance light scattering assay of prostate specific antigen. Biosens Bioelectron. 2012;36(1):35–40.
16. Kong RM, Ding L, Wang ZJ, You JM, Qu FL. A novel aptamer-functionalized MoS_2 nanosheet fluorescent biosensor for sensitive detection of prostate specific antigen. Anal Bioanal Chem. 2015;407(2):369–77.
17. Fang BY, Wang CY, Li C, Wang HB, Zhao YD. Amplified using DNase I and aptamer/graphene oxide for sensing prostate specific antigen in human serum. Sensors Actuators B Chem. 2017;244: 928–33.
18. Choi MS, Yoon M, Baeg JO, Kim J. Label-free dual assay of DNA sequences and potassium ions using an aptamer probe and a molecular light switch complex. Chem Commun. 2009;(47):7419–21.

19. Yang ZR, Wang MM, Wang XS, Yin XB. Boric-acid-functional lanthanide metal-organic frameworks for selective ratiometric fluorescence detection of fluoride ions. Anal Chem. 2017;89(3):1930–6.
20. Qu F, Huang W, You JM. A fluorescent sensor for detecting dopamine and tyrosinase activity by dual-emission carbon dots and gold nanoparticles. Colloids Surf, B. 2018;16:212–9.
21. Haiss W, Thanh NT, Aveyard J, Fernig DG. Determination of size and concentration of gold nanoparticles from UV-Vis spectra. Anal Chem. 2007;79(11):4215–21.
22. Şahin ÇA, Efeçınar M, Şatıroğlu N. Combination of cloud point extraction and flame atomic absorption spectrometry for preconcentration and determination of nickel and manganese ions in water and food samples. J Hazard Mater. 2010;176(1–3):672–7.
23. Cai DN, Guo HL, Wen L, Liu CG. Fabrication of hierarchical architectures of Tb-MOF by a "green coordination modulation method" for the sensing of heavy metal ions. CrystEngComm. 2013;15:6702–8.
24. Gauthier TD, Shane EC, Guerin WF, Seitz WR, Grant CL. Fluorescence quenching method for determining equilibrium constants for polycyclic aromatic hydrocarbons binding to dissolved humic materials. Environ Sci Technol. 1986;20(11):1162–6.
25. Lakowicz JR. Fluorescence sensing. In: Principles of fluorescence spectroscopy. Boston, MA: Springer; 1999. p. 531–72.
26. Tablet C, Hillebrand M. Quenching of the fluorescence of 3-carboxy-5, 6-benzocoumarin by aromatic amines. J Photochem Photobiol, A. 2007;189(1):73–9.
27. Guo JJ, Li HK, Xue M, Zhang MW, Cao XY, Luo YL, et al. Highly sensitive detection of organophosphorus pesticides represented by methamidophos via inner filter effect of Au nanoparticles on the fluorescence of CdTe quantum dots. Food Anal Methods. 2014;7(6):1247–55.
28. Lakowicz JR. Protein fluorescence. In: Principles of fluorescence spectroscopy. Boston, MA: Springer; 1983. p. 341–81.
29. Zheng Y, Wang Y, Yang XR. Aptamer-based colorimetric biosensing of dopamine using unmodified gold nanoparticles. Sensors Actuators B Chem. 2011;15(1):95–9.
30. Zerefos PG, Vougas K, Dimitraki P, Kossida S, Petrolekas A, Stravodimos K, et al. Characterization of the human urine proteome by preparative electrophoresis in combination with 2-DE. Clin Proteomics. 2006;6(15):4346–55.
31. Pauli GEN, de la Escosura-Muñiz A, Parolo C, Bechtold IH, Merkoçi A. Lab-in-a-syringe using gold nanoparticles for rapid immunosensing of protein biomarkers. Lab Chip 2015;15(2):399–405.